

Structure and pressure inside Xe nanoparticles embedded in Al

Konstantin Yakubovskii* and Kazutaka Mitsuishi

Quantum Dot Research Center, National Institute for Materials Science, 3-13 Sakura, Tsukuba 305-0005, Japan

Kazuo Furuya

High Voltage Microscopy Station, National Institute for Materials Science, 3-13 Sakura, Tsukuba 305-0005, Japan

(Received 27 April 2008; published 7 August 2008)

Crystalline and amorphous xenon nanoparticles were produced in aluminum by Xe⁺ ion implantation and were characterized with high-resolution electron microscopy combined with electron energy loss (EEL) spectroscopy. Unusual distributions of the aspect ratio and of the diameter of the crystalline particles were observed and explained, respectively, by minimization of the surface energy and of the strain energy due to the specific lattice mismatch between Al and Xe. Matrix oxidation was revealed as an important phenomenon accompanying the amorphization of Xe particles. Significant variation of relative EEL peak intensities with Xe particle size was observed and associated with unequal pressure inside different particles. The thus revealed variation was utilized to map the pressure distribution inside individual particles with a nanometer spatial resolution.

DOI: [10.1103/PhysRevB.78.064105](https://doi.org/10.1103/PhysRevB.78.064105)

PACS number(s): 68.35.Dv, 61.46.Hk, 61.72.U-, 68.37.Lp

I. INTRODUCTION

Noble gases, introduced by ion implantation or nuclear processes, are insoluble in metals and therefore precipitate into particles.¹⁻⁷ Characterizing the associated phenomena is important both for science and technology. In particular, they have an impact on the development of fusion and fission reactors and help us in understanding the structure of nanoparticles embedded in a crystalline matrix.

Among numerous combinations of the matrix and noble gas element, much attention has been paid to the Al/Xe system for the following reason: Because of the small size of the noble gas precipitates (typically between 1 and 40 nm), they are almost exclusively studied with transmission electron microscopy (TEM). Large difference in the atomic number Z between Xe ($Z=54$) and Al ($Z=13$) results in much stronger electron scattering from Xe that greatly facilitates TEM observations, especially using the high angle annular dark field (HAADF) imaging.² Therefore the Al/Xe system will be the main topic of this paper.

In addition to enhanced TEM observability, Xe particles in Al are remarkable in their structure. Three types of particles usually coexist: crystalline, semicrystalline, and amorphous (see Fig. 1). This variety is understood as follows:^{1,4} the particles are pressurized by the matrix with the pressure increasing as the inverse particle diameter $1/d$. Large particles ($d > 10$ nm) are amorphous (or liquid). At the critical size ~ 10 nm, the pressure reaches 0.41 GPa, which is enough to crystallize Xe at room temperature.⁴ As a result, $d < 10$ nm particles are cubo-octahedral nanocrystals having the same fcc structure as the Al matrix but $\sim 50\%$ larger lattice spacing a ($a_{\text{Xe}} \approx 0.61$ nm and $a_{\text{Al}} = 0.405$ nm). Particles with $d \sim 10$ nm could also be “semicrystalline,” i.e., their center is amorphous, but the top three surface layers are ordered by the interaction with the matrix.¹

The above arguments explained the structure of embedded Xe particles using a single parameter, namely, the particle size and the associated pressure difference. In this paper, we investigate other factors: the matrix oxidation, the difference in the lattice parameter between Xe and Al, and the surface energy of the particles.

The compression of Xe particles by the Al matrix made them a unique object where pressure effects on solid Xe can be investigated at ambient conditions without complex high-pressure equipment, such as a diamond-anvil cell. In this paper, we exploit this advantage in studying the pressure effects on electronic transitions in solid Xe. The latter were

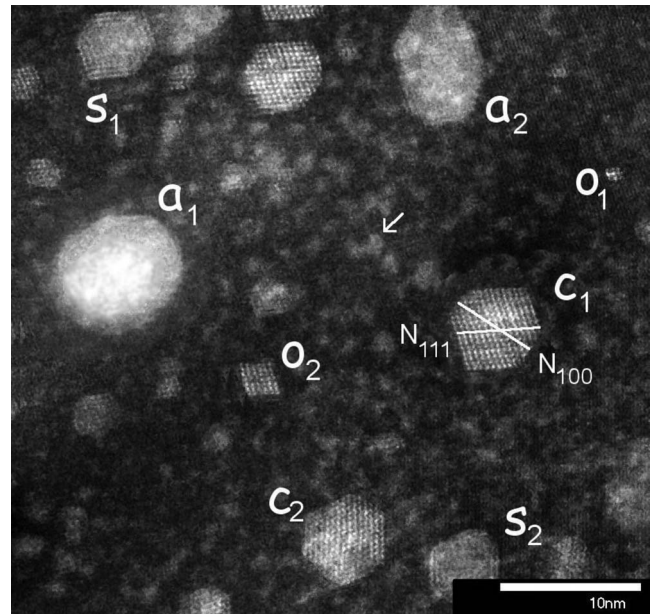


FIG. 1. HAADF STEM image of Xe precipitates in polycrystalline Al (scale bar 10 nm, $\langle 110 \rangle$ axis normal to the picture). Note the coexistence of crystalline ($c_{1,2}$), semicrystalline ($s_{1,2}$), and amorphous ($a_{1,2}$) particles of similar sizes. Crystalline particles exhibit cubo-octahedral or octahedral ($o_{1,2}$) shapes, and the $\langle 110 \rangle$ projection of the particle o_1 contains only nine atoms. The particles in the bottom (c_2 and s_2) and top areas (c_1 , $o_{1,2}$, and s_1) belong to different Al grains; they share a $\langle 110 \rangle$ vertical axis but have different in-plane orientations. The arrow marks one of the numerous small white shapeless features, which do not contain Xe. Drawing over particle c_1 outlines the definition of its normalized aspect ratio $A = N_{100}/2N_{111}$ in terms of the number of (111) and (100) Xe planes.

monitored with electron-energy-loss spectroscopy (EELS) in a scanning transmission electron microscope (STEM). This allowed us not only to characterize individual nanoparticles but also to map, with nanometer spatial resolution, pressure related changes of the electronic structure inside the particles.

II. EXPERIMENTAL DETAILS

Aluminum foils were prepared by electrochemical polishing of well annealed high-purity Al disks. The foils had polycrystalline structure with thickness varying between 20 and 60 nm and with a grain size of a few hundred nanometers. They were implanted with 30-keV Xe⁺ ions to a dose of $\sim 10^{19}$ m⁻² and then annealed at 300 °C for 1/2 h in vacuum in order to remove the residual radiation damage. Microscopic observations and spatially resolved EEL measurements were performed with a 200-keV high-vacuum aberration-corrected Jeol-2500SES scanning STEM (spot size of ~ 0.1 nm) equipped with a Gatan Enfina EEL spectrometer.

III. EXPERIMENTAL RESULTS

A. Crystalline structure of Xe particles and its dependence on the matrix oxidation

Our STEM observations (Fig. 1) revealed a diameter range of ~ 7 – 10 nm where crystalline, semicrystalline, and amorphous Xe particles coexist; in this range, the particle structure does not often follow the diameter-pressure arguments, i.e., larger particles can be crystalline and smaller ones amorphous.

In order to check whether chemical composition can account for this observation, we analyzed the EEL spectra in and around the particles. Apart from the Al and Xe EEL peaks (discussed further in Sec. III D), oxygen *K*-edge signals at ~ 530 eV were detected and chosen for analysis. Their weakness required relatively long acquisition time in order to achieve appropriate signal-to-noise ratio. Therefore, instead of spatial mapping, multiple line scans were performed for a large number of particles, and the representative results are summarized in Fig. 2. They revealed homogeneous oxygen distribution around crystalline and semicrystalline particles and oxygen accumulation around the amorphous ones. This oxygen distribution can be understood as follows: Aluminum surface is covered by ~ 4 nm of natural oxide.⁸ Ion implantation not only introduces Xe but also recoils surface oxygen into the sample. TRIM calculations predict that in a “good quality” crystalline Al matrix covered by 4-nm oxide, the 30-keV Xe ions will be implanted at 21 ± 5 nm and the oxygen will be recoiled into Al to a depth < 1 nm. Therefore, oxygen will not reach Xe particles, and thus their structure will be crystalline (provided their size is < 10 nm and the matrix pressure is sufficient for Xe crystallization). Therefore, the oxygen in the EEL profiles of crystalline (and semicrystalline) particles probably originates from the surfaces of the Al foil. If a large void in Al is created, e.g., as a result of sample preparation or local Al removal due to spatial fluctuations of the ion-beam intensity,

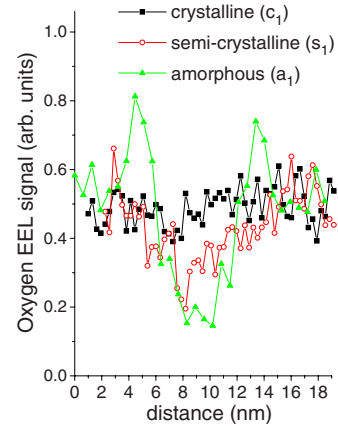


FIG. 2. (Color online) Representative line scans of the integrated oxygen *K*-edge EEL signal acquired across a crystalline (c_1), semicrystalline (s_1), and amorphous (a_1) particles of Fig. 1. Oxygen accumulation at the Xe/Al interface is revealed for the amorphous particles.

then the depth of the oxygen recoil could substantially increase, thus resulting in the oxidation of the void surface. Presence of extended void would reduce the pressure; the latter could become too small for Xe crystallization resulting in amorphous particles. In summary, the oxidation of Al/Xe interface revealed in this paper might not be the primary cause of Xe amorphization, but it is certainly an accompanying process revealing the weakened regions in Al.

B. “Magic numbers” of planes in the crystalline Xe particles

In order to assure the coexistence of different Xe particles in a certain diameter range, dozens of high-resolution HAADF STEM images were processed, and the results are presented in Figs. 3 and 4. The histogram of Fig. 3(a) not only confirms the coexistence range of ~ 7 – 10 nm but also reveals an unusual oscillatory diameter distribution of the crystalline particles. In Fig. 3(b), we have reanalyzed the data of Fig. 3(a) in terms of the number of Xe (111) and (100) planes rather than the corresponding *distances*. Such analysis reduces errors originating from the imperfect microscope calibrations, sample misalignment, and inaccurate choice of directions along the particle. An oscillatory behavior was confirmed such that the even number of planes was observed more frequently than the odd ones.

Note that an oscillatory diameter distribution has been observed for Pb particles in Al.^{9,10} It was successfully explained by minimization of the strain energy originating from the lattice mismatch between Pb and Al, and we have adopted below that model to the Al/Xe system.

Dashed line in Fig. 3(b) presents a corresponding simulation of the (111) histogram using a product of a Gaussian and Boltzmann distributions as

$$\exp[-(N_{111} - 11)^2/70 - \alpha V \Omega^2/kT]. \quad (1)$$

Here N_{111} is the number of (111) planes, V is the particle volume, $\alpha = 18 \text{ K } \mu / (3 \text{ K} + 4 \mu) \cong 18 \text{ K} / 4 \approx 9 \text{ GPa}$ for Xe,¹¹ μ is the shear modulus of Al, and K is the bulk modu-

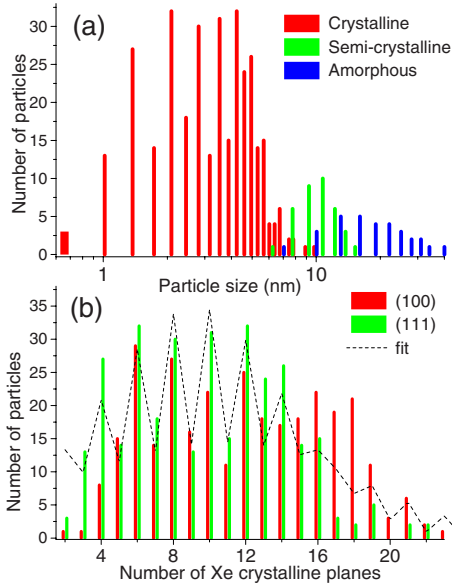


FIG. 3. (Color online) Histograms of Xe nanoparticles in Al as a function (a) of the particle size and (b) of the number of Xe (111) or (100) crystalline planes. Note a coexistence of crystalline, semi-crystalline, and amorphous particles in the diameter range 7–10 nm (a). Details of fitting the (111) distribution [dashed line in (b)] are outlined in the text.

lus of Xe. The first (Gaussian) term accounts for the scarcity of large and small crystalline Xe particles. Its apparent overestimate of the number of small particles is partly due to the elevated difficulty of their experimental detection. The second (Boltzmann) term contains the strain energy $E_S = \alpha V \Omega^2$. The Moiré-fringe function $\Omega = \min_p |p \cdot a_{Al} / a_{Xe} - N_{111}|$, where

p is an integer, accounts for the lattice mismatch between the host and guest crystals. In case of Pb in Al the mismatch is only 20%, and thus the period of $\Omega(N_{111})$ oscillations is relatively large (~ 8 lattice planes). However, for Xe in Al the mismatch is $\sim 50\%$ and the $\Omega(N_{111})$ period is about two lattice planes only. Continuous models, such as strain model, might not work in such a clearly discrete case, and thus the observation of a two-plane period for Xe in Al is not trivial.

C. Aspect ratio of the crystalline Xe particles

We have also analyzed the distributions of Fig. 3 in terms of the normalized aspect ratio A . In order to improve the accuracy of measurements, it was defined as (see Fig. 1) $A = N_{100}/2N_{111}$, i.e., in terms of the number of (111) and (100) planes rather than corresponding distances.¹⁰ For analysis purposes, this normalized aspect ratio is plotted as a function of the particle volume rather than the number of planes. The $A(V)$ plot of Fig. 4 exhibits an unusual asymmetry such that larger aspects are preferred to the smaller ones, and the spread is decreasing with the particle volume. Following Gibbs,¹² this interesting behavior can be explained by minimizing the energy of the Al/Xe interface at fixed particle volume as follows: The interface energy E_{if} of a cubo-octahedron can be expressed⁴ as a function of the aspect ratio and volume,

$$E_{if} = \sqrt{3} \gamma_{111} V^{2/3} \frac{1 - 3(1 - \gamma_{100}/\sqrt{3}\gamma_{111})(1-A)^2}{[1 - 3(1-A)^2]^{2/3}}. \quad (2)$$

Here γ_{100} and γ_{111} are the interface tensions for the corresponding planes, $\gamma_{100}/\gamma_{111} = 1.05$.⁴ Figure 4(b) demonstrates that E_{if} is an asymmetric function of A that naturally explains the asymmetry of the $A(V)$ distribution of Fig. 4(a). The maximum deviation of A can be found by a simple graphical procedure of defining maximum energy fluctuations [horizontal dashed line in Fig. 4(b)] and deducing the corresponding extremal A_e values for each particle volume. The thus deduced $A_e(V)$ dependences [dashed lines in Fig. 4(a)] agree well with the experiment.

Note that the total energy of a Xe particle in Al includes several terms, such as the edge, vertex, interface, and strain energies. The former two can be neglected but the latter two are essential.¹⁰ However, in our analysis we have selected only the strain energy for Fig. 3(b) and the interface energy for Fig. 4(a) because of the following reasons: As confirmed by the analysis of Fig. 4(a), the interface energy [Eq. (2)] accounts for the shape (aspect ratio) of Xe particles. It was not included in the fitting of Fig. 3(b) [Eq. (1)] because the figure—for reasons of increasing the experimental accuracy—is presented vs the number of planes, and the shape information there is hidden in the difference between the (111) and (100) distributions. On the other hand, minimization of the strain energy [Eq. (1)] explains why certain numbers of Xe planes are preferred [see Fig. 3(b)]. However, strain energy is only a minor high-frequency component as compared to the interface energy.^{10,13} It will not affect significantly the maximum range of the aspect ratio, which is being fitted in Fig. 4(a). Note also that the interface energy alone has been treated semicontinuously [see Fig. 4(b)];

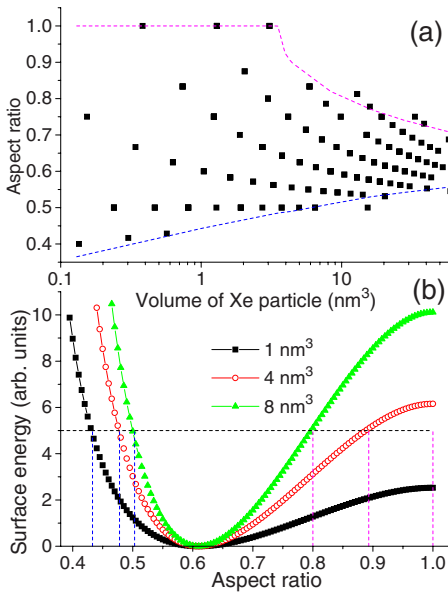


FIG. 4. (Color online) Top panel: the aspect ratio A , defined in Fig. 1, as a function of the volume of the crystalline Xe particles in Al. Bottom panel: surface energy calculated for three particles; minimum energy is set at zero. The energy fluctuations (horizontal dashed line) define the maximal range of A values ($A \leq 1$), which is presented by lines in the top panel.

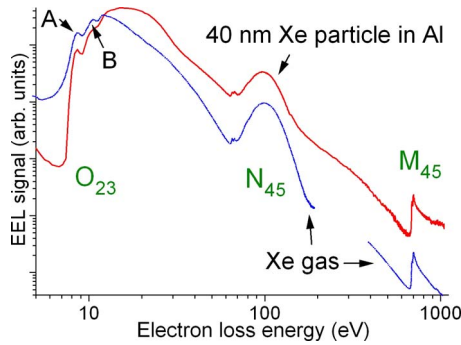


FIG. 5. (Color online) Electron energy-loss spectrum from an amorphous 40-nm Xe particle in Al and a Xe gas reference spectrum (Ref. 14), both measured with ~ 0.8 eV resolution. The spectra are plotted in a double-logarithmic scale for presentation purposes. Symbols O_{23} , N_{45} , and M_{45} conventionally identify the associated atomic transitions, while A and B label the peaks used in the pressure measurements discussed below.

however, if the (discrete) strain energy is included, then the particle volume cannot be fixed and a more complex minimization approach should be used.¹⁰

D. Effect of pressure on the electronic transitions in Xe particles

Similar to optical absorption, EEL spectroscopy probes electronic structure via electronic transitions induced by the incident electron beam.¹⁴ In connection with Xe, it is instructive to consider first a reference gas spectrum¹⁴ shown by the blue line in Fig. 5. Three bands are observed, originating from transitions between discrete atomic levels and conventionally labeled O_{23} , N_{45} , and M_{45} . In this study, we shall focus on the two O_{23} features labeled as A and B .

Strong matrix contributions hampered the previous EEL studies of noble gas nanoparticles.⁵⁻⁷ In this paper, matrix signals were minimized by selecting thin regions where large (up to 40 nm) Xe particles were surrounded by a few nanometer thin Al layer. A representative spectrum is shown by the red curve in Fig. 5; it is similar to the Xe gas spectrum; however, an extra broad peak is observed at ~ 20 eV. The latter is associated with plasmon excitations and is a unique feature distinguishing solid Xe from gas.¹⁵ Relative intensities of the A and B peaks varied from particle to particle, but the comparison of the absolute intensities was hampered by different amounts of Xe. In order to compensate for this effect, we have selected isolated round particles and normalized their spectra to the particle diameter. Normalization revealed (see Figs. 6 and 7) that the intensity of peak A was constant but the strength of peak B increased with decreasing particle size. This observation naturally explains the anomalous B/A ratio reported previously.^{6,7}

Regarding the origin of this intensity variation, we would first note that it was independent of the particle crystallinity. Thus the crystal symmetry contribution is insignificant here. Interface effects are important because the ratio of “surface” to “bulk” atoms is larger for smaller bubbles. Therefore, we have remeasured the spectra of Fig. 6, focusing the ~ 0.1 nm probe into the center or the edge of the particle, relying on

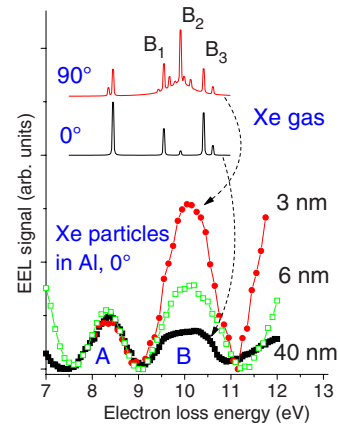


FIG. 6. (Color online) Bottom part: lines and symbols show background subtracted EEL spectra from Xe particles in Al with the sizes 3, 6, and 40 nm. Second-order polynomials were used as the baselines and the spectra are normalized to the particle diameter. Top part: lines show a reproduction of the high-resolution EEL spectra from Xe gas (Ref. 16) measured in 0° and 90° scattering geometries. The 90° spectrum reveals an extra strong forbidden peak B_2 , which explains the variation of the B -peak intensity with Xe particle size.

that many more interface atoms will be sampled in the latter case. No significant difference was observed, thus suggesting minor role of Al/Xe interfaces in this case. In particular, we did not observe coupling to the “bubble surface plasmon” possibly because of the larger sizes of our Xe particles (>3 nm compared to ~ 1 nm of Refs. 6 and 7).

Continuous variation of the B/A peak ratio with the particle size prompted pressure effects. Therefore we have converted the particle size into pressure¹⁷ and added a pressure scale in Fig. 7. This procedure revealed quadratic increase in the B/A ratio with the pressure.

In order to assert pressure effects on our EEL spectra it is again instructive to analyze the Xe gas spectra. The gas spectrum of Fig. 5 was recorded at low resolution for comparative purposes; better resolved spectra are reproduced in the top part of Fig. 6. They were recorded in another study¹⁶ at 0° and 90° scattering angles that enhanced dipole-allowed

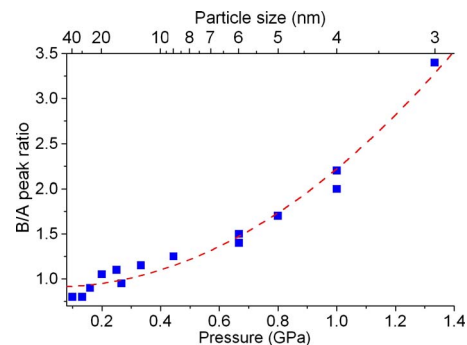


FIG. 7. (Color online) Solid squares present the ratio of B to A EEL peak intensity (see Figs. 5 and 6) as a function of particle size. The latter has been converted into pressure inside the particles using the previously reported data (Ref. 17). Dashed line is a second-order polynomial fit.

and dipole-forbidden transitions, respectively. The selectivity is however not perfect, and the allowed lines appear in the 90° spectrum. Those spectra reveal the multiplet structure of the peak B dominated by a forbidden line B_2 and allowed lines B_1 and B_3 .

Because of obvious technical difficulties, pressure dependence of EEL spectra has not been studied previously. However, effect of pressure on electronic transitions, *regardless of how they are induced*, is well known. In particular, pressure mixes the electronic transitions of similar energies; if one of them was dipole forbidden, then it could become (partly) allowed and its intensity will increase nonlinearly with the pressure. A representative example is the 0.396 (allowed) and 0.401 eV (forbidden) electronic transitions in ZnO.¹⁸ Moderate pressures (<0.5 GPa) increase the intensity of the latter from zero to half of that of the former, and the increase is quadratic with the pressure. Insignificant line shift is observed, meaning that for two states to become mixed their energies do not have to become equal or even change much.

The above arguments can explain the results of Figs. 6 and 7 as follows: Increasing internal pressure mixed B_1 , B_2 , and B_3 transitions, thus making allowed the forbidden peak B_2 and strengthening the integral B peak. This interpretation is supported by the quadratic pressure dependence of the induced peak intensity (see Fig. 7) and by the shape of the B peak (see bottom part of Fig. 6): At small pressures (particle size 40 nm), its flat top suggests an unresolved B_1/B_3 doublet, while at larger pressures (sizes 3 or 6 nm), the pointed shape appears as an unresolved B_{1-3} triplet. Note that the line shapes are unresolved here possibly not because of the insufficient spectral resolution but because of solid-state and strain related broadening. Indeed, the B_{1-3} peaks could not be separated in solid Xe films even when measured with high-resolution spectrometers.^{19,20}

E. Mapping pressure inside individual Xe nanoparticles

The observations of Figs. 6 and 7 bring us to a remarkable conclusion that electronic properties and pressure in Xe nanoparticles can be mapped with a subnanometer spatial resolution of TEM. As a test, we have monitored the pressure distribution inside Xe particles in Al as outlined in Fig. 8. Its top part is a HAADF STEM image showing several round and elongated amorphous bubbles. The latter originated from incomplete aggregation of individual particles, as revealed in previous *in situ* experiments.³ The A and B EEL peaks were measured at every image point; their ratio was converted into the pressure using Fig. 7 and was plotted in the bottom panel. This panel reveals that the pressure is homogeneous in the individual round bubbles but not in the elongated aggregates. This pressure inhomogeneity could originate from several effects, such as residual stresses, incomplete bubble aggregation, or presence of Al or Al oxide membranes separating the particles.²¹ The analysis of associated phenomena is beyond the scope of this paper, and the underlying physics could be relatively trivial. However, the demonstration that electronic

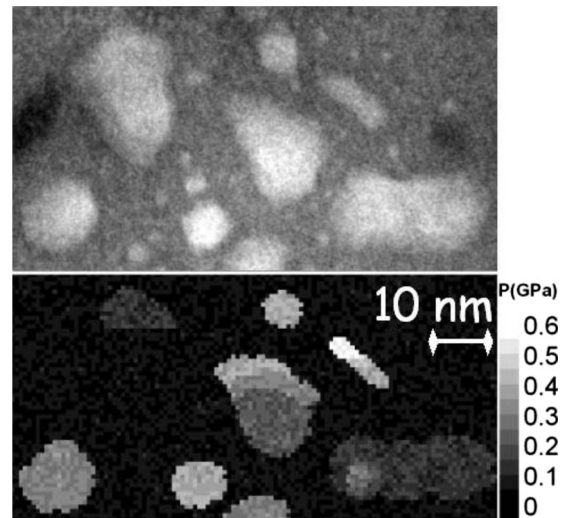


FIG. 8. Top panel: high angle annular dark field image of Xe nanoparticles (white features) in Al. Bottom panel: map of pressure inside the particles (in GPa) deduced from the B/A EEL peak intensity ratio (see Figs. 6 and 7). Note that the top left particle exploded during the scan and that the pressure inside the smallest particles could not be deduced because of the large thickness in this sample area.

properties of (noble gas) nanoparticles and the associated pressure effects can be monitored at room temperature with subnanometer spatial resolution is important.

IV. SUMMARY AND CONCLUSIONS

Crystalline Xe nanoparticles in Al exhibit unusual distributions of their diameter and aspect ratio, which can be explained by minimization of the strain and surface energies, respectively. The particle crystallinity can be associated with the matrix oxidation, which was neglected previously.

Background-free EEL spectra from individual Xe nanoparticles demonstrate that the *electronic* structure of the particles, in the first approximation, does not differ from that of solid Xe. However, the relative intensities of the low-energy EEL peaks exhibit systematic changes with the particle size well into the nanometer range. This phenomenon is explained by the variation in the internal pressure, which mixes allowed and forbidden EEL transitions thereby altering their intensities. The relative peak intensities were applied to map the pressure inside individual Xe nanoparticles, and nanometer scale resolution has been achieved. The thus developed approach is not limited to Xe in aluminum and can be applied to a wide range of nanostructures.

ACKNOWLEDGMENTS

The authors are grateful to S. E. Donnelly for a useful discussion. This research was partially supported by Ministry of Education, Science, Sports, and Culture (MEXT) through the grant in aid for Young Scientists (B) 2005 17710120-6816, World Premier International Research Center Initiative on Materials Nanoarchitectonics, and the Nuclear Research Project.

*iakoubovskii.konstantin@nims.go.jp

- ¹S. E. Donnelly, R. C. Birtcher, C. W. Allen, I. Morrison, K. Furuya, M. Song, K. Mitsuishi, and U. Dahmen, *Science* **296**, 507 (2002).
- ²K. Mitsuishi, M. Kawasaki, M. Takeguchi, and K. Furuya, *Phys. Rev. Lett.* **82**, 3082 (1999).
- ³R. C. Birtcher, S. E. Donnelly, M. Song, K. Furuya, K. Mitsuishi, and C. W. Allen, *Phys. Rev. Lett.* **83**, 1617 (1999).
- ⁴C. W. Allen, R. C. Birtcher, S. E. Donnelly, M. Song, K. Mitsuishi, K. Furuya, and U. Dahmen, *Philos. Mag. Lett.* **83**, 57 (2003).
- ⁵K. Furuya, K. Mitsuishi, M. Song, and T. Saito, *J. Electron Microsc.* **48**, 511 (1999).
- ⁶A. vom Felde and J. Fink, *Phys. Rev. B* **31**, 6917 (1985).
- ⁷A. vom Felde, J. Fink, T. Muller-Heinzerling, J. Pfluger, B. Scheerer, G. Linker, and D. Kaletta, *Phys. Rev. Lett.* **53**, 922 (1984).
- ⁸T. Campbell, R. K. Kalia, A. Nakano, P. Vashishta, S. Ogata, and S. Rodgers, *Phys. Rev. Lett.* **82**, 4866 (1999).
- ⁹U. Dahmen, S. Q. Xiao, S. Paciornik, E. Johnson, and A. Johansen, *Phys. Rev. Lett.* **78**, 471 (1997).
- ¹⁰J. C. Hamilton, F. Leonard, E. Johnson, and U. Dahmen, *Phys. Rev. Lett.* **98**, 236102 (2007).
- ¹¹J. R. Packard and C. A. Swenson, *J. Phys. Chem. Solids* **24**, 1405 (1963).
- ¹²J. W. Gibbs, *Trans. Conn. Acad. Arts Sci.* **3**, 343 (1878).
- ¹³Note that for Xe in Al $\gamma_{111} \approx 1.05 \text{ J/m}^2$, $\alpha \approx 9 \text{ GPa}$ (Refs. 4 and 11) but for Pb in Al $\gamma_{111} \approx 0.445 \text{ J/m}^2$, $\alpha \approx 96 \text{ GPa}$ (Refs. 9 and 10). Therefore the ratio of strain energy to interface energy is ~ 25 times smaller for the Al/Xe than for the Al/Pb system.
- ¹⁴*Transmission Electron Energy Loss Spectrometry in Material Science and the EELS Atlas*, edited by C. C. Ahn (Wiley, Weinheim, Germany, 2004).
- ¹⁵J. D. Nuttall, T. E. Gallon, M. G. Devey, and J. A. D. Matthew, *J. Phys. C* **8**, 445 (1975).
- ¹⁶A. Delage and J. D. Carette, *Phys. Rev. A* **14**, 1345 (1976).
- ¹⁷M. Song, K. Mitsuishi, K. Furuya, C. W. Allen, R. C. Birtcher, and S. E. Donnelly, *J. Microsc.* **215**, 224 (2004).
- ¹⁸E. V. Lavrov and J. Weber, *Phys. Status Solidi B* **243**, 2657 (2006).
- ¹⁹J. E. Demuth, P. Avouris, and D. Schmeisser, *Phys. Rev. Lett.* **50**, 600 (1983).
- ²⁰K. Wandelt, W. Jacob, N. Memmel, and V. Dose, *Phys. Rev. Lett.* **57**, 1643 (1986).
- ²¹R. J. Cox, P. J. Goodhew, and J. H. Evans, *J. Nucl. Mater.* **126**, 117 (1984).